A novel positively-charged metal-coordinated nanofiltration membrane for lithium recovery

Li Wang[a,b], Danyal Rehman[c], Peng-Fei Sun[d], Akshay Deshmukh[c], Liyuan Zhang[b], Qi Han[a], Zhe Yang[b*], Zhongying Wang[a*], Hee-Deung Park[d], John H. Lienhard[c*] and Chuyang Y. Tang[b]

[a] School of Environmental Science and Engineering, Southern University of Science and Technology, Shenzhen 518055, China

[b] Department of Civil Engineering, the University of Hong Kong, Pokfulam, Hong Kong, SAR, P. R. China

[c] Department of Mechanical Engineering, Massachusetts Institute of Technology, Cambridge MA 02139, USA

[d] School of Civil, Environmental and Architectural Engineering, Korea University, Seoul, 02841, South Korea

[*] to whom correspondence should be addressed.

Zhongying Wang e-mail: wangzy6@sustech.edu.cn; tel.: +86-075588018040;

Zhe Yang e-mail: zheyang@connect.hku.hk; tel.: +852-2857 8470;

John H. Lienhard e-mail: lienhard@mit.edu.; tel.: +1-617-253-3790

Keywords:

Lithium recovery; copper-MPD; nanofiltration; high permeance and high selectivity; pH-responsive; antimicrobial properties

Abstract

Nanofiltration (NF) if with high water flux and precise separation performance with high Li^{+}/Mg^{2+} selectivity, is ideal for lithium brine recovery. However, conventional polyamide-based commercial NF membranes are ineffective in lithium recovery processes due to their undesired Li^{+}/Mg^{2+} selectivity. In addition, they are constrained by the water permeance-selectivity trade-off, which means that highly permeable membrane often has lower selectivity. In this study, we developed a novel non-polyamide NF membrane based on metal coordinated structure, which exhibits simultaneously improved water permeance and Li^{+}/Mg^{2+} selectivity. Specifically, the optimized Cu-m-phenylenediamine (MPD) membrane demonstrated a high water permeance of 16.2 ± 2.7 LMH/bar and a high Li^{+}/Mg^{2+} selectivity of 8.0 ± 1.0, which surpassed the trade-off of permeance-selectivity. Meanwhile, the existence of copper in the Cu-MPD membrane further enhanced antibiofouling property and the metal-coordinated nanofiltration membrane possesses a pH-responsive protperty. Finally, a transport model based on the Nernst-Planck equations has been developed to fit the water flux and rejection of uncharged solutes to the experiments conducted. The model had a deviation below 2% for all experiments performed and suggested an average pore radius of 1.25 nm with a porosity of 0.21 for the Cu-MPD membrane. Overall, our study provides an exciting approach for fabricating non-polyamide high-performance nanofiltration membrane in the context of lithium recovery.

INTRODUCTION

Lithium, the lightest metal, has been extensively applied in rechargeable batteries with numerous important applications such as environmental-friendly vehicles, mobile communication equipment and other electric devices.[1] Lithium can be extracted from aqueous media including salt lakes, brines, and seawater, of which continental brine accounts for approximately ~ 59% of the worldwide lithium production.[2, 3] Therefore, many technologies have been developed to recover lithium from aqueous sources.[4-8] Compared to conventional approaches such as solar evaporation, chemical precipitation, adsorption, and solvent extraction, nanofiltration (NF) offers a promising alternative thanks to its simplicity, low energy consumption, and nontoxicity to the environment.[9-14]

NF is a pressure-driven membrane separation technology,[15] with a molecular weight cut-off (MWCO) ranging from 200 to 1000 Da. Commercial NF membranes adopt a thin-film composite (TFC) structure, where an ultra-thin polyamide rejection layer is formed on the microporous substrate with an interfacial polymerization reaction. The polyamide layer has a charged surface, ensuring an efficient separation of mono- and multi-valent ions at low operating pressures.[11, 16] Nanofiltration in lithium recovery is mainly employed as a pretreatment of the brine to eliminate the unwanted solutes (e.g., magnesium), with a subsequent evaporation process to precipitate and crystallize lithium-related products.[3] Therefore, the high lithium selectivity is preferred to improve the product purity. In addition, high permeance could further translate into enhanced lithium production. Consequently, NF has been extensively studied for lithium recovery from brine.[17] Nevertheless, conventional polyamide-based NF membranes are inefficient for achieving more precise membrane selectivity[18, 19] and are adversely constrained by a trade-off between water permeance and selectivity, *i.e.,* higher water permeance resulting in lower selectivity and vice versa.[10, 20-25]

Given the fact that the permselectivity limits of the polyamide chemistry, exploring non-polyamide materials is critical to overcoming the longstanding tradeoff between water permeance and selectivity.[10, 23, 24, 26, 27] MPD, which, along with trimesoyl chloride (TMC), is one of the key monomers in the fabrication of polyamide RO membranes, has dominated the RO market since its discovery. However, the highly-crosslinked MPD-TMC polyamides used in RO membranes have a relatively low water permeance of 1-3 LMH/bar[10] and a high rejection of both Li^+ and Mg^{2+},[3] limiting their effective separation. For instance, Uyuni salar brine contains 15-18 g/L Mg and 0.7-0.9 g/L Li,[28] where Mg can interfere the lithium recovery process by competing with Li in the formation of carbonate precipitate. It is difficult for commercial membrane to selectively remove Mg^{2+} from the brine mixture due to their comparable hydrated radius (Mg of 0.428 nm vs. Li of 0.382 nm).[13] Therefore, we envisage an NF membrane fabricated by the self-polymerization of MPD assisted by Cu^{2+}. Cu^{2+} promots the polymerization and crosslinking and also serves as the positive-charge-center in the NF membrane. Moreover, this fabricating scheme of Cu-MPD membrane can be readily integrated with the existing production line of commercial TFC membrane.

In this study, we fabricated a non-polyamide NF membrane featuring a positively-charged rejection layer consisting of Cu-MPD complexes. The Cu-MPD complexes imparts the membrane with concurrently high water permeance and enhanced the Mg^{2+}/Li^{+} selectivity. Due to the low rejection of lithium ions by the Cu-MPD membrane, there would not be significant lithium dilution to increase the energy consumption in the process of precipitation. Furthermore, a highly-permeable membrane could potentially reduce the energy consumption for the pretreatment by lowering the operation pressure.[29] Meanwhile, the pH-responsive nature of the Cu-MPD membrane enables further tuning of water permeance and rejection, showing great potential in lithium recovery application. The fabricated membrane successfully exceeded the state-of-art upper bound pertaining lithium recovery. Our work shall have some insights into future membrane designs in the context of lithium recovery.

MATERIALS AND METHODS

Materials and Chemicals

Deionized (DI) water was produced by Millipore system (Millipore, Billerica, MA) and used for the preparation of all solutions. Polyethersulfone (PES) ultrafiltration substrate (UH050, MWCO 50 kDa) was purchased from Microdyn Nadir. *m*-phenylenediamine (MPD, flakes, 99%, Sigma-Aldrich), $CuCl_2·2H_2O$ (Macklin, China), $NaIO_4$ (99.5%, Macklin, China) and glutaraldehyde (GA, 50% in water, Aladdin China) were used for fabricating membrane rejection layer. LiCl (anhydrous, 98%) and $MgCl_2·6H_2O$ (98%) was purchased from Tokyo Chemical Industry (TCI, Japan) and Uni-Chem, respectively. D-(+) Glucose (Mw. 180.16, Diekmann), D-(+) sucrose (Mw. 342.3, Diekmann) and dextran (Mw 1000 and 2000, D-chem) were used for the evaluation of membrane pore size. Absolute ethanol (≥99.8%) was purchased from NORMAPUR VWR, Dorset, U.K. All chemicals are analytical grade unless noted otherwise.

Fabrication of Cu-MPD NF membrane

As shown in Figure 1a, the fabrication protocol of the Cu-MPD NF membrane is illustrated as follows: a piece of PES substrate (20 × 12 cm) was rinsed with DI water and mounted into a home-made shaking reactor. First, a certain concentration of MPD solution was added into the reactor with continuous shaking for 2 min to wet the substrate surface. Then, $CuCl_2$ solution (1 wt% in DI water) was introduced into the MPD solution to form the Cu-MPD complexes for 2 min. To accelerate the polymerization, $NaIO_4$ solution (4 wt% in DI water) was then added into the mixture and shaken for 5 h at 100 rpm. The membrane was taken out and immersed in DI water overnight to remove the excessive chemicals. Afterwards, the membrane was crosslinked in GA solution (2 wt% in ethanol solution) at 50 ºC for 20 min.[30, 31] Subsequently, the membrane was taken out from the GA ethanol solution and put in an oven of 50 ºC for another 20 min for post-treatment.[30] The resultant NF membrane is denoted as CuX-MPD-NF, where X represents the mass ratio of Cu to MPD varied from 0, 1/3, 1/2, 1 and 2.

Membrane Characterization

Surface morphologies of the Cu-MPD NF membrane and PES substrate were examined by field emission scanning electron microscopy (FE-SEM, S-4800, Hitachi) at 5 kV. Transmission electron microscopy (TEM, Philips CM100, 100 kV) was utilized to obtain cross-sectional images of the surface layer of the resultant membrane. Prior to characterization, membrane samples were embedded in a resin (Epon, Ted Pella, CA), which was subsequently cut by an Ultracut E ultramicrotome (Reichert, Inc. Depew, NY) into slices with a thickness of around 100 nm. These slices then were placed on a copper grid and characterized in TEM. Atomic force microscopy (AFM, Veeco, Nanoscope IIIa Multimode) was used to evaluate membrane surface morphology and roughness. X-ray photoelectron spectroscopy (XPS, Leybold Sengyang, China) was ultilized to analyze the surface chemical compositions of the membranes. Water Contact angle (Attension Theta, Biolin Scientific Sweden) was employed to measure the water contact angle of the prepared membranes. The streaming potential (SurPASS 3 Electrokinetic Analyzer, Anton PaarGmbH, Austria) was used for testing membrane surface charge. A quartz crystal microbalance with dissipation (QCM-D, E4, QSense Biolin Scientific, Sweden) was applied to examine the structure and mass change of the MPD-Cu complexes.[32] Considering the sensitivity of QCM-D technique, the step of GA crosslinking was omitted in the preparation of Cu-MPD complexes on the gold sensor. However, the QCM-D measurements adopted the polymerization reaction between Cu^{2+} and MPD, which allows us to reveal the important role of solution pH on affecting the structure and water adsorption properties of Cu-MPD complexes. Therefore, the detailed preparation procedures are described as follows: First, Cu1/2-MPD complex was synthesized by the reaction 40 mL 2% MPD, 40 mL 2% $CuCl_2$ and 20 mL 4% $NaIO_4$, with a polymerization time of 5 hr. The complex solution was further diluted 1000 times, and 100 uL of the diluted solution was added onto a gold-coated quartz wafer. Please note that no GA was added for cross-linking due to the limitation of gold sensor. Afterwards, the coated wafer was placed in oven at 60^{o}C overnight for drying. Furthermore, three of the coated wafers were placed in three parallel flow cells in the QCM-D chamber. To initiate the test, pure water was infiltrated into the QCM-D flow cells for 10 min to rinse and stabilize the system and then brines of pH 3, 7, 9 with a concentration of 2000 ppm ($MgCl_2$ and LiCl mixture) were pumped into cells to investigate the pH responsive behavior of the complex (Figure 4a). The frequency and dissipation variation of the three wafers were recorded.

We further employed QCM-D open cell to investigate of the mechanism of the membrane formation (Figure S6b). First, 200 μL of certain concentration of MPD solution diluted by 10 times was added into the cell and stabilized for a period of time, and then 200 μL of 0.2% $CuCl_2$ was added into it and wait until the frequency of the system stabilized. Finally, 200 μL 0.4% $NaIO_4$ was rapidly added into the cell. The system was further left for reaction until there was no change in the frequency was observed. The frequency was recorded during the whole process and was converted into the thickness of the developed membrane on the surface of the wafer through a Sauerbrey equation.

The mechanism of QCM-D was described as follows: with a set of QCM-D equipment, one can measure the frequency and dissipation value of the system. The frequency variation can be further converted into mass change or thickness change of the system by a Sauerbrey equation. On the other side, the dissipation value of the coated materials can further translate into the structural change of the membrane.[33]

Separation Performance Testing

A cross-flow filtration setup was used to test the separation performance of the membranes. Water permeance and rejection were measured at 5 bar at room temperature, and each membrane was pre-pressured at 6 bar for 2 h to reach the steady-state. Water flux can be calculated according to Eq. (1),

$$J_w = \frac{\Delta V}{\Delta t \times A} \quad (1)$$

where J_w (L m^{-2} h^{-1}) is the pure water flux; ΔV (L) is the volume of permeate; A (m^2) is the active membrane area and Δt (h) is the sampling time.

For the rejection measurement, 1000 ppm $MgCl_2$ was used as feed solution. A conductivity meter was used to measure the conductivity of permeate and feed to determine the salt concentrations and then rejection defined by Eq. (2),

$$\text{Rej}_i = 1 - \frac{C_p}{C_f} \quad (2)$$

where R is the salt rejection, while C_p and C_f are the salt concentrations of the permeate and feed solution, respectively.

To examine the performance of the membranes in the application of Li recovery from brine, a synthetic brine with a concentration of 2000 ppm (Mg/ Li mass ratio of 23) was used as the feed solution and pH of the feed was adjusted from 3 to 9 using diluted HCl and NaOH solutions.[34] Thus the separation factor $S_{Li,Mg}$ was calculated by Eq. (3),

$$S_{Li,Mg} = \frac{C_{Li,p}/C_{Mg,p}}{C_{Li,f}/C_{Mg,f}} \quad (3)$$

where $S_{Li,Mg}$ is the separation factor of Li^+ over Mg^{2+}, $C_{Li,p}$ and $C_{Li,f}$ are the Li^+ concentration in permeate and feed, respectively, $C_{Mg,p}$ and $C_{Mg,f}$ are the Mg^{2+} concentration in permeate and feed, respectively. Inductive coupled plasma optical emission spectrometer (ICP-OES, Optima 8 × 00, PerkinElmer) was used to measure the concentration of Li^+ and Mg^{2+} according to our previous work.[32]

Nanofiltration model for uncharged solutes

The Donnan-Steric Pore model (DSPM) was used to develop a framework to characterize transport across the fabricated Cu-MPD nanofiltration membranes.[35-39] The extended Nernst-Planck equation was applied to model transmembrane transport. For uncharged solutes, the migration term is neglected and transport is governed by convection and diffusion.[40] The resulting expressions are integrated across the membrane yielding closed-form expressions for individual solute fluxes. Water transport is calculated using the Hagen-Poiseuille equation for flow through a tortuous cylindrical pore, in line with observed membrane morphologies. The water and solute fluxes are decoupled and provided by Eq. (4) and Eq. (5), respectively: [37, 39, 41, 42]

$$J_v = \frac{\epsilon r_p^2 \Delta P}{8\tau\eta L} \quad (4)$$

$$N_i = \frac{H_{i,C} J_v c_{i,F}}{1-(1-H_{i,C})\exp(-\mathrm{Pe}_i)} \quad (5)$$

In Eq. (4), J_v is the volumetric water flux, ϵ is the porosity, r_P is the effective pore radius, τ is the tortuosity, and η is the dynamic viscosity. Across the membrane, ΔP is the applied hydraulic pressure and L is the membrane thickness. A membrane thickness of 0.5 μm was assumed in this work, based on the cross-sectional SEM images of the Cu-MPD membrane active layer (Figure S1). In Eq. (5), N_i is the molar flux of solute i, which is a function of its convective hindrance factor, $H_{i,C}$, Péclet number, Pe_i, and feed concentration, $c_{i,F}$. The permeate concentration of each solute, $c_{i,P}$, is given by molar solute flux divided by the the volumetric solvent flux.

The Péclet number captures the ratio of convective to diffusive hindrance factors across the membrane and is defined in Eq. (6):

$$\mathrm{Pe}_i = \frac{K_{i,c} J_v L}{K_{i,d} D_i} \qquad (6)$$

where, $K_{i,d}$ is the diffusive hindrance coefficient and D_i is the diffusion coefficient of the solute in the solvent. In high Péclet number regimes, convection dominates and the solute flux is primarily governed by the convective hindrance factor, the water flux, and the concentration of the permeate. Conversely, in low Péclet number regimes, the solute rejection is diffusion limited and only depends on the solute flux and permeate concentration.

Hindrance parameters are usually written as functions of the relative penetrant size, λ_i, where λ_i is defined as the ratio of the solutes' Stokes-Einstein radii to the membrane effective pore radius.[43, 44] In this work, the convective and diffusive hindrance processes are assumed to exhibit activated-type or Arrhenius-like behavior whereby $K_{i,c}$ and $K_{i,d}$ are exponential functions of the convective and diffusive fitting parameters, $\alpha_{i,c}$ and $\alpha_{i,d}$, respectively.[18, 45-48] The mathematical expressions for $K_{i,c}$ and $K_{i,d}$ are given by:

$$K_{i,c} = \exp\left(-\alpha_{i,c}\lambda_i\right) \quad (7)$$

$$K_{i,d} = \exp\left(-\alpha_{i,d}\lambda_i\right) \quad (8)$$

The semi-empirical parameters $\alpha_{i,c}$ and $\alpha_{i,d}$ in Eq.s (7) and (8) reflect the averaged, temperature-normalized energy barrier associated with solute convection and diffusion processes, respectively. These parameters were used along with the membrane porosity and effective pore radius are determined by the regression of experimental data to the model for uncharged solutes.

Rejection of each solute species $(1 - c_{i,P}/c_{i,F})$ is given by: [37, 39, 41]

$$\mathrm{Rej}_i = 1 - \frac{H_{i,C}}{1-\left(1-H_{i,C}\right)\exp(-\mathrm{Pe}_i)} \quad (9)$$

where Rej_i is the rejection of solute species *i*. In addition to fitting the rejection of each solute, the model was also fit to the water flux measurements conducted as detailed in Section 2.4. A particle swarm algorithm implemented in Matlab (Mathworks, Natick, MA) was used to minimize the normalized least squared residual between the model and experiments for all uncharged solutes: glucose, sucrose, dextran (1 kDa), and dextran (2 kDa). [37, 39, 41] The objective function and fitted design variables are provided in Eq. (10).

$$\mathrm{Obj} = \min_{\epsilon, r_P, \alpha_{i,c}, \alpha_{i,d}} \left\{ \sum_{k=1}^{n_f} \left(\frac{J_{v,k}^{\mathrm{mod}} - J_{v,k}^{\mathrm{exp}}}{J_{v,k}^{\mathrm{exp}}} \right)^2 + \sum_{i=1}^{n_s} \left[\sum_{k=1}^{n_f} \left(\frac{\mathrm{Rej}_{i,k}^{\mathrm{mod}} - \mathrm{Rej}_{i,k}^{\mathrm{exp}}}{\mathrm{Rej}_{i,k}^{\mathrm{exp}}} \right)^2 \right] \right\} \quad (10)$$

where the superscripts mod and exp denote the model and experiments. n corresponds to the number of data points collected, where the subscripts s and f denote the experimental data points representing solute rejection and water flux, respectively.

Anti-biofouling test

Pseudomonas aeruginosa PA14 was used as the model gram-negative bacteria for all anti-biofilm and anti-biofouling assays. Approximately 15 mL of tryptic soy broth (TSB) (BD, NJ, USA) was inoculated with a single colony of *P. aeruginosa* and cultured in a shaking incubator at 37 °C and 250 rpm overnight.[49] Cells were then centrifuged at 4 °C and 8000 rpm for 10 min, washed and suspended with sterile PBS for the following tests.

Anti-biofilm experiments were carried out using a rotating disk biofilm reactor (DK20, Biosurface, Montana, USA) under medium shear conditions. Briefly, the membrane coupons were taped on the rotating disk. The biofilm was firstly formed in batch mode (no flow) for 24 h with 1 mL PA14 suspension (10^6 CFU/mL) and 250 mL TSB solution (300 mg/L). After reaching steady-state growth, the reactor was operated for an additional 24 h with a continuous flow of the TSB solution (30 mg/L, 8.5 mL/min). During the whole biofilm formation, the membrane coupon surfaces were continuously exposed with fluid shear from the rotation of the disk (200 rpm). At the end, the membrane coupons were removed from the disk for confocal laser scanning microscopy (CLSM) (LSM700, Carl Zeiss, Jena, Germany) observation and viable cell enumeration. [50, 51]

In addition, the anti-biofouling tests were conducted using a cross-flow membrane module. A 4 L synthetic wastewater was recirculated using a high-pressure pump (Hydra-cell pump, Wanner Engineering, Minneapolis, MN) with a flow rate of 1 L/min and pressure of 5 bar. Following cleaning and stabilization, the biofouling experiments were initiated by injecting bacterial suspension (10^7 CFU/mL) into the feed tank. After anti-biofouling, the membranes were carefully removed from the module for CLSM analysis.

RESULTS AND DISCUSSION

Microscopic analysis and surface properties of the membranes.

Figure 1 presents the proposed chemical structure of the MPD-Cu complexes.[52] Briefly, MPD was self-polymerized and initiated by Cu^{2+} and $NaIO_4$ to form Cu-MPD complexes, and GA was used to improve the crosslinking degree of the resulting membrane.[31, 53] Specifically, Cu^{2+} could promote this self-polymerization by coordinating with MPD monomers and mediating the transfer of electrons from MPD to $NaIO_4$.[52] In addition, Cu^{2+} serves as the positive-charge center in the resultant complexes. After the MPD monomer is oxidized, it becomes a cationic radical and cleave from the coordination. The generated radical would further attack a free MPD monomer to propagate the polymer chain. Simultaneously, another free MPD monomer would occupy the vacancy of the remaining radical and start a cycle of oxidation and polymerization, resulting in a propagating polymer chain. To confirm the formation of the positively charged Cu-MPD complexes, zeta potential measurements of the plain PES and Cu-MPD membranes were performed. As shown in Figure S2, the PES substrate was negatively charged throughout the pH range between pH 3 to 9. In contrast, the Cu-MPD NF membrane exhibited increased positive-charge density in the pH range from 3 to 7.4 (the isoelectric point). The positive-charge property on the surface of the membrane can be potentially ascribed to the Cu-MPD complexes containing cationic copper and protonated amino groups at acidic to neutral conditions.

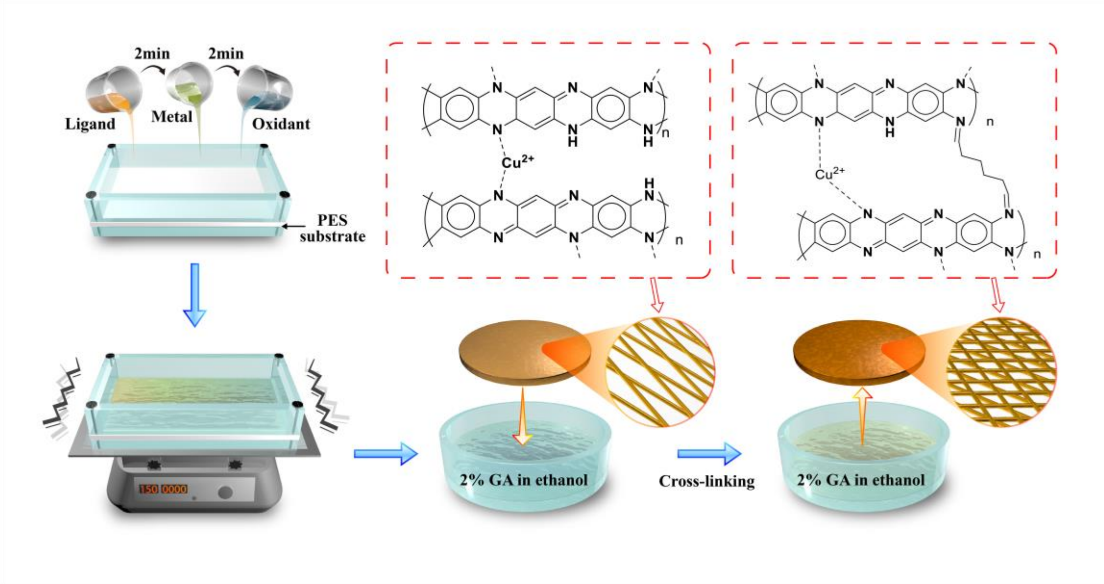

Figure 1. Membrane fabrication route and structural illustration of Cu-MPD NF membrane. MPD, $CuCl_2$ and $NaIO_4$ solution was poured onto the surface of the PES substrate, successively, followed by immersion of the surface-coated membrane into a GA/ethanol bath at 50 °C to form crosslinked Cu-MPD NF membrane. The volume of the MPD, $CuCl_2$ and $NaIO_4$ solution were 80, 80, 40 mL, respectively.

To further confirm the formation of the Cu-MPD complexes, SEM and TEM techniques were applied to examine membrane surface and cross-section morphologies. As shown in Figure 2a, the pristine PES substrate had a flat surface (with root-mean-square roughness R_q of 12.2 nm in Figure 2e), with evenly distributed nanosized pores.[54] After coating the Cu-MPD complexes, the substrate pores vanished with numerous nodules prevailing on the surface of the Cu-MPD membrane (Figure 2c) with increased R_q of 22.1 nm in Figure 2f), which is in good agreement with the literature.[52] Cu-MPD membranes with different components (Table S1) and various Cu/MPD ratios were fabricated, and their morphologies and topographies were characterizated through SEM (Figure S1a) and AFM (Figure S3). From there we can see that such nodules were absent when no Cu^{2+} or $NaIO_4$

involved in the coating process, confirming the indispensable roles of Cu^{2+} and $NaIO_4$ in promoting the formation of Cu-MPD complexes.[55]

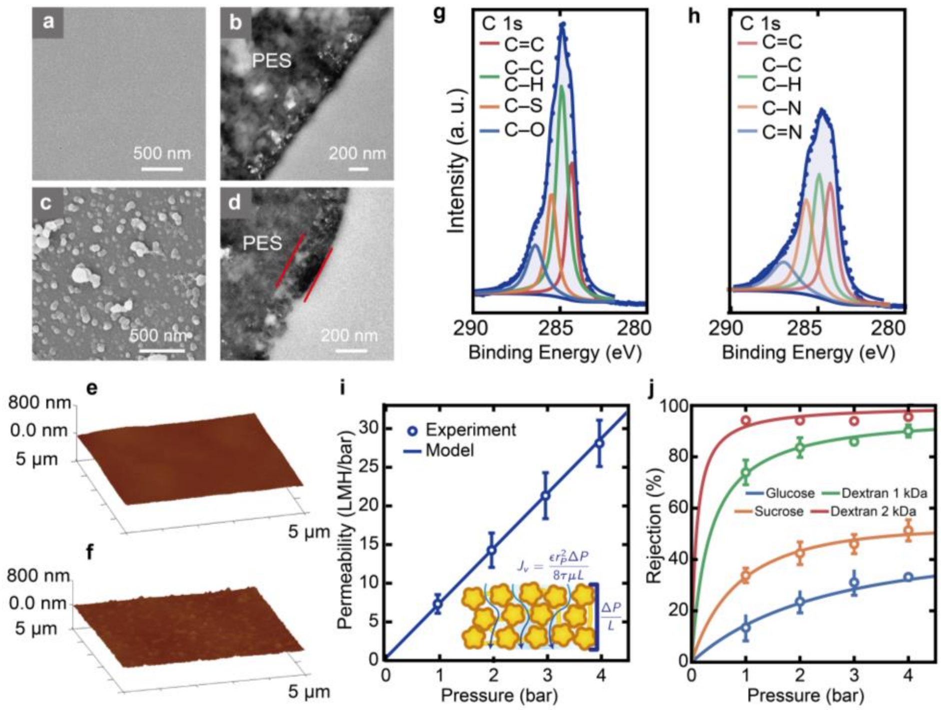

Figure 2. (a-b) SEM, (c-d) TEM, (e-f) AFM and (g-h) XPS of the prepared membrane; (a, b, e, g) are for PES substrate, and (c, d, f, h) are for Cu1/2-MPD NF membrane. (i) water flux against applied pressure; (j) rejection of neutral solutes under different applied pressure for the Cu1/2-MPD membrane. For (i, j), dots are data obtained from experimental work, and curves are model work.

TEM (Figure 2(b,d)) images present the cross-sections of the pristine PES substrate and the Cu-MPD membrane. Compared to PES, the Cu-MPD membrane had a thick-rejection layer of several hundred nanometers (marked between the two red lines in Figure 2d). XPS was also used to confirm the formation of the Cu-MPD membrane on the surface of the PES substrate (Figure 2(g,h) and Figure S4(a-c)). Results in Figure 2(g,h) show the C 1s spectra of the PES substrate and the

Cu1/2-MPD membrane to reveal the chemical compositions of the synthesized complex structure. Specifically, the deconvolution of C 1s spectrum of the PES substrate (Figure 2g) showed four peaks at 284.4, 284.9, 285.3 and 286.1 eV, attributed to the C=C, C-C, C-S and C-O of the backbone of the PES structure, respectively.[56] In contrast, C-N and C=N were also detected in the Cu1/2-MPD membrane at the bonding energy of 285.1 and 287.0 eV, respectively, in addition to the peaks related with C=C and C-C of the polymerized MPD chain (Figure 2h).[53, 57] N 1s spectrum was also investigated for the Cu1/2-MPD membrane to gain further information of the membrane composition (Figure S4b). The peak at 399.4 eV indicated the -NH, while the peak at 399.9 and 400.1 eV can be assigned to -N= and -N-C, respectively. In addition, the signal of 401.1 eV indicates the presence of $-N^{+}=$, which can be due to the coordination of Cu^{2+} and amino groups on the Cu-MPD polymer chain.[53] The existence of Cu can also ben verified by the zeta potential (Figure S4d) and isoelectric point data (Table S2), where the isoelectric point of membrane Cu1/2-MPD was pH 7.4 ± 0.2 while for Cu0-MPD it was pH 5.3 ± 0.3. Overall, the structural and compositional characterizations above demonstrate the successful synthesis and loading of positively charged Cu-MPD onto a PES substrate.

To better understand the structure of the novel NF membrane, we use a DSPM-DE model to characterize membrane porosity and pore radius. Figure 2i shows the modeled and experimentally-measured water flux as a function of the applied hydraulic pressure. A linear relationship is observed between water flux and hydraulic pressure. The model, which is based on a Hagen-Poiseuille formulation, aligns very strongly with the experiments. In Figure 2j, the rejection of each species is plotted as a function of the applied hydraulic pressure. The DSPM-derived model is able to capture the experimentally-observed variation of the solute rejection for all the solutes tested across the range of hydraulic pressures analyzed. Solute rejection increases with penetrant size in alignment with the physical intuition underlying size-based selectivity. The rejection of each solute initially increases rapidly with transmembrane pressure, before plateauing.[37, 39, 41] The increase in observed rejection is driven by an increase in water flux, which leads to an increase in convective hindrance. As transmembrane water flux continues to increase, solute rejection approachs the high Péclet limit where $\mathrm{Rej}_i \rightarrow 1 - H_{i,C}$. The fitted porosity and effective pore radius obtained from the global optimization method were 0.21 and 1.25 nm, respectively. Conventional nanofiltration membranes have porosities and effective pore radii that range from 0.02-0.1 and 0.5-2 nm, respectively.[40, 58-62] The regressed parameters suggest that the Cu-MPD membranes are significantly more porous than conventional nanofiltration membranes, which aligns with observations from the SEM and TEM images taken. The effective pore radius, however, is similar to current polyamide membranes. Lastly, the alignment between the model and experimental data highlights the model's predictive capabilities in determining the rejection of uncharged solutes coordination-complex-based membranes.

Separation properties and lithium recovery performances of the membranes.

Figure 3 presents the effect of Cu/MPD ratio on the separation performance of the membranes. The actual copper loading concentration in membrane fabricated with various Cu/MPD ratio was characterized with EDX (Figure S5) and ICP-OES (Table S4).Without copper, the membrane exhibited relatively low rejection (22.6 ± 2.4%) with low water permeance (1.3 ± 0.1 LMH/bar). With the increased Cu/MPD ratio, an improved membrane water permeance and simultaneously enhanced $MgCl_2$ rejection up to 90.0 ± 1.2% was observed. An optimized Cu/MPD ratio appears to be between 1/2 and 1, with the ratio of Cu/MPD strongly affecting the polymerization of Cu-MPD complexes and therefore affecting their surface morphologies (Figure S1). We speculate that the absence of copper led to the formation of incomplete and loose MPD complex layer as Cu can promote the MPD self-polymerization.[52] Such a loose structure could be further severely compacted at high transmembrane pressure, leading to low water permeance and low $MgCl_2$ rejection. When Cu/MPD ratio increased, the structure of the formed Cu-MPD complex became more rigid with fewer defects, resulting in improved membrane separation performance. As the ratio exceeded 1, however, synthesized Cu-MPD complex exhibited different assembly pathways and decreased thickness as demonstrated by the different oligomer absorption peaks in Figure S6a and QCM-D measurements in Figure S6b. This might give some insight in explaining that the membrane exhibited an optimal structure with Cu/MPD ratio varying 1/2 to 1. Separation performance of more membranes fabricated with different components can be seen in Figure S7.

We further selected Cu1/2-MPD membrane as a benchmark to perform the lithium recovery test from brine, and found its high Li^+/Mg^{2+} selectivity and high water permeance (Figure 3(b,c)). Specifically, the pH of feed solution was varied from 3 to 9 to reveal the pH-dependent lithium recovery performance. Interestingly, unlike the conventional polyamide-based NF membrane encountering the water permeance-selectivity trade-off,[10] the Cu-MPD membrane demonstrated both high water permeance of 16.2 ± 2.7 LMH/bar and high rejection against LiCl and $MgCl_2$ of 32.3 ± 7.6% and 91.6 ± 0.2%, respectively, at pH 3. The more pronounced enhancement for rejecting divalent ions of $MgCl_2$ further led to a high Li^+/Mg^{2+} selectivity value (8.0 ± 1.0, Figure 3b), which can be potentially due to the enhanced Donnan exclusion effect, resulted from more protonated amino groups at lower pH solution. At pH 9, in contrast, the membrane had systematically decreased water permeance of 9.1 ± 0.7 LMH/bar and reduced rejection of LiCl and $MgCl_2$ of 21.7 ± 2.1% and 78.9 ± 0.5%, respectively. Consequently, their Li^+/Mg^{2+} selectivity decreased to 3.9 ± 0.1, potentially due to the neutralized membrane surface. As a result, the high-performance Cu-MPD membrane at pH 3 showed relatively good performance in the correlation in the upper bound diagram between membrane water permeance and Li/Mg selectivity for the state-of-the-art NF membrane, including both lab work and commercial membranes (Figure 3d, Figure S11 and Table S3).[63] It is worthnoting that testing conditions (e.g., operating pressure, feed concentration, temperature and etc.) do affect membrane separation performance. In order to exclude the effect of operating conditions, the correlation between water-salt permselectivity A/B_{MgCl2} vs. membrane permeance A and salt-salt selectivity B_{LiCl}/B_{MgCl2} vs. membrane permeance A to examine membrane intrinsic transport properties were plotted in the revised Supporting Information (Figure S11).

The pH of the feed solution would greatly affect the charge density of the membrane active layer by changing the protonation condition of the amino groups in the Cu-MPD complex. Specifically, when pH increases, fewer amino groups are protonated, leading to reduced positive charge density of membrane active layer; As a result, the electrostatic repulsion between these amino group decreases, leading to a tighter structure of the Cu-MPD complex. Therefore, the pore size of the membrane is reduced, and vice versa. When pH decreased, more amino groups became protonated, leading to higher positive charge-density. This electrostatic repulsion would result in a looser structure of the Cu-MPD complex. Thus, more water could be captured and enter the nano pores of the Cu-MPD complex.

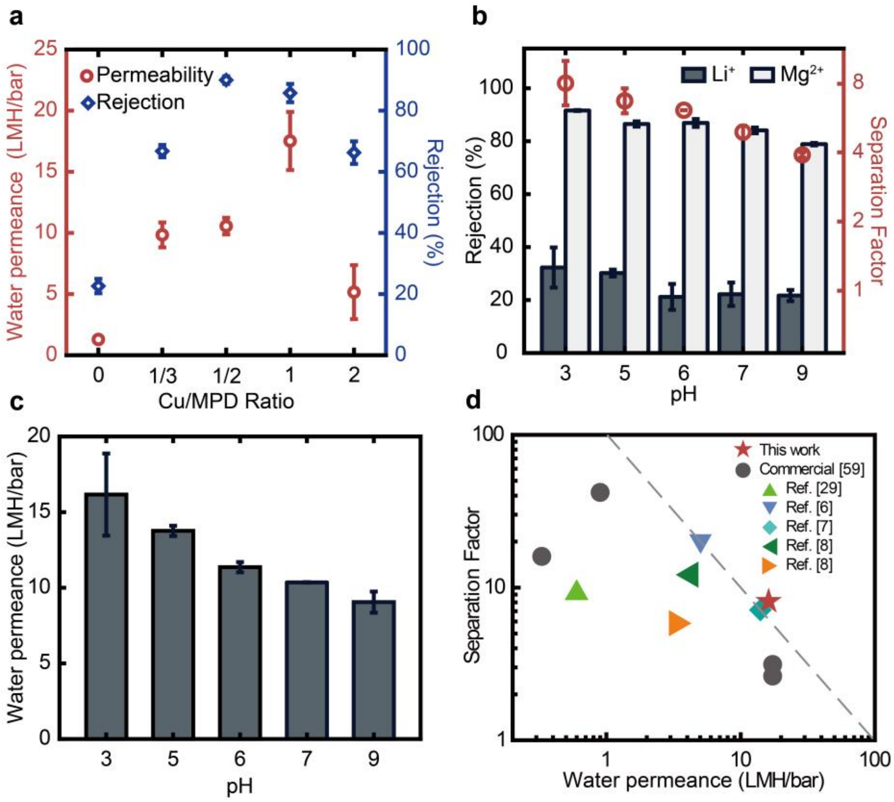

Figure 3. Separation properties and lithium recovery performances of the Cu-MPD membranes. (a) Water permeance and Mg^{2+} rejection of membrane fabricated at varied Cu/MPD ratios, (b) lithium recovery performance of Cu-MPD NF membrane as a function of pH. Membrane rejection of Li^{+}, Mg^{2+} and separation factor (*S*) of Li^{+}/Mg^{2+} and (c) pure water permeance in the pH range from 3-9 and (d) the performance boundary between water permeance and Li^{+}/Mg^{2+} separation factor, including literature results, commercial membranes and the membrane developed from this study. All filtration tests are operated at 5 bar, 1000 ppm of $MgCl_2$ was used for evaluating membrane rejection for Mg^{2+} and a synthetic brine of a concentration of 2000 ppm (Li/Mg mass ratio of 23) was used for evaluating membrane lithium recovery performance. All the presented results are based on three membrane coupons replicates.

Mechanisms of the pH-responsive properties of the membranes.

To gain a better understanding of the pH-responsive membrane properties, we further performed QCM-D analysis on the structure and mass change of the Cu-MPD membranes under different pH conditions. A significant decrease in frequency was observed when pH decreased from 9 to 3 shown in Figure 4a, implying an increased mass of Cu-MPD membrane. Such an increase is caused by more-opening pore structure that could accomodate more water molecules and ions. Indeed, the highest Dissipation (D) value was obtained for the Cu-MPD complexes at pH 3, thanks to the enhanced electrostatic repulsion for the protonated amino groups at a lower pH. The looser structure further explains the enhanced water absorption (Figure 4a) as well as the improved membrane water permeance (Figure 3b). On the contrary, a higher pH resulted in both decreased changes in D and frequency (F) values, corresponding to a more rigid layer structure and a lower water absorption, respectively. This can be potentially due to the diminished charge interaction, which can be certified by the zeta potential results shown in Figure S2.

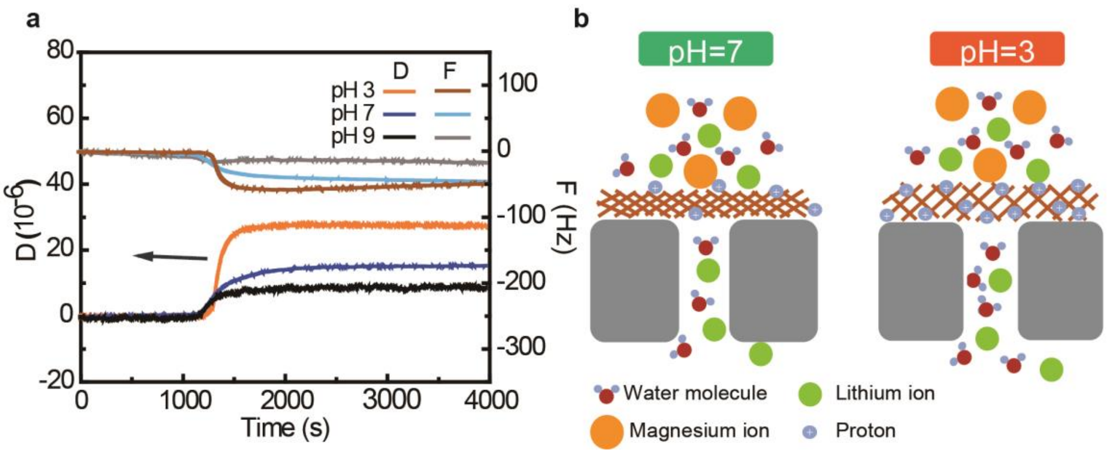

Figure 4. (a) QCM-D characterization of Cu-MPD NF membrane using simulated brine of 2000 ppm at pH 3, 7 and 9. Cu/MPD complexes at ratio of 1/2 were coated on the surface of the gold senor. To perform the charaterization, DI water was first filtrated through the system for stabilizing. Subsequently, brine with different pH was introduced with the real-time measured frequency and dissipation and (b) a schematic illustration of a mechanism for pH-responsive membrane.

Antibiofouling properties of the membranes.

Conventional polyamide-based NF membranes are prone to biofouling and significantly increase its operation costs.[32] Copper is a well-known antimicrobial agent.[64, 65] In this regard, antibiofouling and antimicrobial properties of the Cu-MPD membrane were investigated. The CLSM images (Figure 5b) show reduced biofilm thickness after a 10 h filtration test for the copper-contained membrane compared to the control counterpart. Moreover, compared to the control membrane showing significant water flux loss, the Cu-MPD membrane exhibited only a slightly reduced water flux thanks to the antifouling capability as a result of the loaded copper (Figure 5a). We further performed the significance test for the two groups of data of colony forming unit (Supporting Information Figure S8), and the calculated p value is 0.03, implying a significant antimicrobial ability of the membrane with copper relative to that without copper. We also performed static antimicrobial tests using the rotating disc reactor. After 40 h rotating disc experiment, the Cu-MPD membrane and control were taken out from the reactor for CLSM imaging (Figure S9a), which showed that fewer live bacteria can be observed on the surface of Cu-MPD membrane in line with the anti-biofouling tests. In addition, more live bacteria were observed on the plate spread with bacteria suspension solutions from control, compared to that of Cu-MPD membrane (Figure S8(b,c)).

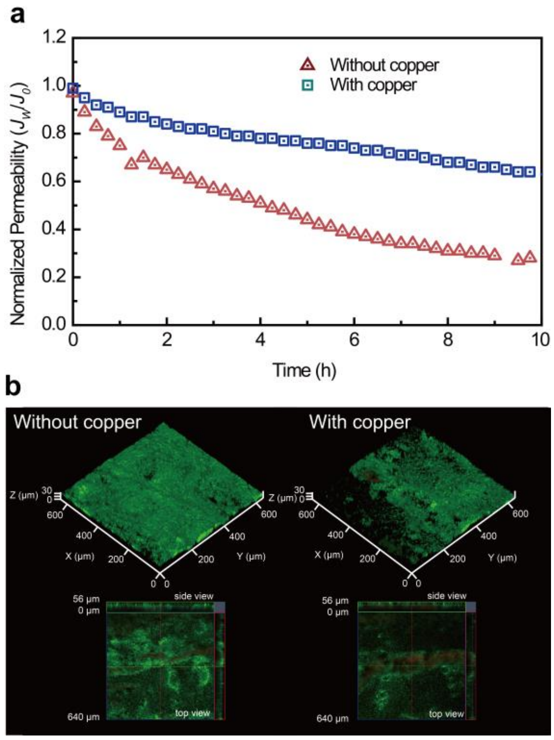

Figure 5. Anti-biofouling tests of the membranes with and without copper using a cross flow filtration system and rotating disc reactor. (a) normalized membrane water flux with and without copper, (b) CLSM image of the membrane surface with and without copper after 10 h filtration at 10 bar.

CONCLUSION

We developed a novel non-polyamide NF membrane with Cu^{2+} assisted MPD self-polymerization. The fabrication conditions and the effect of Cu^{2+} on membrane structure and separation performance were systematically investigated. The optimized membrane exhibited high water permeance and high Li^{+}/Mg^{2+} selectivity, which exceeded the upper bound of the lab-made membrane as well as commercial membranes. Furthermore, the membrane showed both increased water permeance and salt rejection at lower pH. The underlying mechanism in membrane structure and surface charge density at different pH was elucidated with the aid of QCM-D. An NF model was also developed in this work to fit water flux and rejection of uncharged solutes to experimental data. The model was within a 2% deviation of all conducted experiments. Lastly, the Cu-MPD NF membrane showed good anti-biofouling ability, accounted for its Cu^{2+} loading and surface positive charge. The high porsity and suitable pore radius implied by modelling and separation performance highlight the great promise of Cu-MPD membranes in the fields relevant to NF applications. Additionally, this method can be further extended by tuning pore size using different monomers or cations for versatile applications, such as heavy metal removal and dye retention.

ASSOCIATED CONTENT

The Supporting Information is available free of charge at DOI:

SEM images and photos of prepared membranes; Zeta potential of Cu-MPD NF membrane and PES substrate; AFM images of prepared membranes; XPS spectra and zeta potential of prepared membranes; Copper loading in prepared membrane with different Cu/MPD ratios; UV-vis spectra and thickness of Cu-MPD oligomers with different Cu/MPD ratios; Separation performance of membrane with different components; Membrane anti-biofouling ability test by rotating disc; Membrane anti-biofouling ability test by cross-flow filtration; Copper leaching test in pure water; Comparison of membrane filtration performance in this work to the literature; Membrane long-term running stability test; Feed, retentate and permeate concentration in 12h filtration; The recipe for fabricating the Cu-MPD membrane; Contact angle and isoelectrical point of prepared membranes; Comparison of this work to the literature; Cu loading concentration in different types of membranes; Average biofilm thickness and average biovolume on surface of prepared membranes; I and Cu concentration before and after 5h reaction; Performance of membrane with different recipes; The recipe of the membranes in Table S7.

AUTHOR INFORMATION

Corresponding Authors

Zhongying Wang e-mail: wangzy6@sustech.edu.cn; tel.: +86-075588018040;

Zhe Yang e-mail: zheyang@connect.hku.hk; tel.: +852-2857 8470;
John H. Lienhard e-mail: lienhard@mit.edu.; tel.: +1-617-253-3790

Authors

Li Wang: 0000-0001-9829-4729
Danyal Rehman: 0000-0001-9457-191X
Peng-Fei Sun: 0000-0002-3942-9766
Akshay Deshmukh: 0000-0002-3693-1902
Liyuan Zhang: 0000-0002-7585-5607
Qi Han: 0000-0003-3493-0655
Zhe Yang: 0000-0003-0753-3902
Zhongying Wang: 0000-0002-7869-6859
Hee-Deung Park: 0000-0002-5769-335X
John H. Lienhard: 0000-0002-2901-0638
Chuyang Y. Tang: 0000-0002-7932-6462

Notes

The authors declare no competing financial interest.

ACKNOWLEDGMENTS

This study was supported by the General Research Fund (Preject number: 17204220) of the Research Grants Council of Hong Kong. This work was also supported by National Nature Science Foundation of China (No. 22076075) and the Centers for Mechanical Engineering Research and Education at MIT and SUSTech (MechERE Centers at MIT and SUSTech). The authors acknowledge the assistance of SUSTech Core Research Facilities.

References:

1. Goriparti, S.; Miele, E.; De Angelis, F.; Di Fabrizio, E.; Proietti Zaccaria, R.; Capiglia, C., Review on Recent Progress of Nanostructured Anode Materials for Li-Ion Batteries. *J. Power Sources* **2014,** *257*, 421-443.
2. Swain, B., Recovery and Recycling of Lithium: A Review. *Sep. Purif. Technol.* **2017,** *172*, 388-403.
3. Li, X.; Mo, Y.; Qing, W.; Shao, S.; Tang, C. Y.; Li, J., Membrane-based technologies for lithium recovery from water lithium resources: A review. *J. Membr. Sci.* **2019,** *591*, 117317.
4. Zhao, X.; Yang, H.; Wang, Y.; Sha, Z., Review on the Electrochemical Extraction of Lithium from Seawater/brine. *J. Electroanal. Chem.* **2019,** *850*, 1572-6657.
5. Li, X.; Zhang, C.; Zhang, S.; Li, J.; He, B.; Cui, Z., Preparation and Characterization of Positively Charged Polyamide Composite Nanofiltration Hollow Fiber Membrane for Lithium and Magnesium Separation. *Desalination* **2015,** *369*, 26-36.
6. Xu, P.; Wang, W.; Qian, X.; Wang, H.; Guo, C.; Li, N.; Xu, Z.; Teng, K.; Wang, Z., Positive charged PEI-TMC composite nanofiltration membrane for separation of Li+ and Mg2+ from brine with high Mg2+/Li+ ratio. *Desalination* **2019,** *449*, 57-68.
7. Zhang, H.-Z.; Xu, Z.-L.; Ding, H.; Tang, Y.-J., Positively charged capillary nanofiltration membrane with high rejection for Mg2+ and Ca2+ and good separation for Mg2+ and Li+. *Desalination* **2017,** *420*, 158-166.
8. Guo, C. S.; Li, N.; Qian, X. M.; Shi, J.; Jing, M. L.; Teng, K. Y.; Xu, Z. W., Ultra-Thin Double Janus Nanofiltration Membrane for Separation of Li^+ and Mg^{2+}: "Drag" Effect from Carboxyl-containing Negative Interlayer. *Sep. Purif. Technol.* **2020,** *230*, 115567.
9. Quist-Jensen, C. A.; Ali, A.; Drioli, E.; Macedonio, F., Perspectives on Mining from Sea and Other Alternative Strategies for Minerals and Water Recovery-the Development of Novel Membrane Operations. *J. Taiwan Inst. Chem. Eng.* **2019,** *94*, 129-134.
10. Yang, Z.; Guo, H.; Tang, C. Y., The upper bound of thin-film composite (TFC) polyamide membranes for desalination. *J. Membr. Sci.* **2019,** *590*, 117297.
11. Zhang, Y.; Wang, L.; Sun, W.; Hu, Y.; Tang, H., Membrane Technologies for Li^+/Mg^{2+} Separation from Salt-Lake Brines and Seawater: A Comprehensive Review. *J. Ind. Eng. Chem.* **2020,** *81*, 7-23.
12. Ahdab, Y. D.; Rehman, D.; Lienhard, J. H., Brackish Water Desalination for Greenhouses: Improving Groundwater Quality for Irrigation Using Monovalent Selective Electrodialysis Reversal. *J. Membr. Sci.* **2020,** *610*, 118072.
13. Wen, X.; Ma, P.; Zhu, C.; He, Q.; Deng, X., Preliminary study on recovering lithium chloride from lithium-containing waters by nanofiltration. *Sep. Purif. Technol.* **2006,** *49*, (3), 230-236.
14. Ahdab, Y. D.; Rehman, D.; Schücking, G.; Barbosa, M.; Lienhard, J. H., Treating Irrigation Water Using High-Performance Membranes for Monovalent Selective

Electrodialysis. *ACS ES&T Water* **2020,** *1*, 117-124.

15. Guo, H.; Peng, L. E.; Yao, Z.; Yang, Z.; Ma, X.; Tang, C. Y., Non-Polyamide Based Nanofiltration Membranes Using Green Metal-Organic Coordination Complexes: Implications for the Removal of Trace Organic Contaminants. *Environ. Sci. Technol.* **2019,** *53*, (5), 2688-2694.

16. Yang, Z.; Ma, X.-H.; Tang, C. Y., Recent development of novel membranes for desalination. *Desalination* **2018,** *434*, 37-59.

17. Somrani, A.; Hamzaoui, A. H.; Pontie, M., Study on Lithium Separation from Salt Lake Brines by Nanofiltration (NF) and Low Pressure Reverse Osmosis (LPRO). *Desalination* **2013,** *317*, 184-192.

18. Epsztein, R.; DuChanois, R. M.; Ritt, C. L.; Noy, A.; Elimelech, M., Towards Single-Species Selectivity of Membranes with Subnanometre Pores. *Nature Nanotech.* **2020,** *15*, (6), 426-436.

19. Sarkar, P.; Modak, S.; Karan, S., Ultraselective and Highly Permeable Polyamide Nanofilms for Ionic and Molecular Nanofiltration. *Advanced Functional Materials* **2021,** *31*, (3), 2007054.

20. Robeson, L. M., Correlation of Separation Factor versus Permeability for Polymeric Membranes. *J. Membr. Sci.* **1991,** *62*, (2), 165-185.

21. Robeson, L. M., The Upper Bound Revisited. *J. Membr. Sci.* **2008,** *320*, (1-2), 390-400.

22. Geise, G. M.; Park, H. B.; Sagle, A. C.; Freeman, B. D.; McGrath, J. E., Water Permeability and Water/Salt Selectivity Trade-Off in Polymers for Desalination. *J. Membr. Sci.* **2011,** *369*, (1-2), 130-138.

23. Geise, G. M.; Paul, D. R.; Freeman, B. D., Fundamental Water and Salt Transport Properties of Polymeric Materials. *Prog. Polym. Sci.* **2014,** *39*, (1), 1-42.

24. Werber, J. R.; Deshmukh, A.; Elimelech, M., The Critical Need for Increased Selectivity, not Increased Water Permeability, for Desalination Membranes. *Environ. Sci. Technol. Lett.* **2016,** *3*, (4), 112-120.

25. Roy, Y.; Lienhard, J. H., A Framework to Analyze Sulfate versus Chloride Selectivity in Nanofiltration. *Environ. Sci.: Water Res. Technol.* **2019,** *5*, (3), 585-598.

26. Park, H. B.; Kamcev, J.; Robeson, L. M.; Elimelech, M.; Freeman, B. D., Maximizing the Right Stuff: The Trade-Off between Membrane Permeability and Selectivity. *Science* **2017,** *356*, (6343), 1137.

27. Werber, J. R.; Osuji, C. O.; Elimelech, M., Materials for Next-Generation Desalination and Water Purification Membranes. *Nat. Rev. Mater.* **2016,** *1*, (5), 1-15.

28. Meshram, P.; Pandey, B. D.; Mankhand, T. R., Extraction of lithium from primary and secondary sources by pre-treatment, leaching and separation: A comprehensive review. *Hydrometallurgy* **2014,** *150*, 192-208.

29. Yang, Z.; Sun, P.-F.; Li, X.; Gan, B.; Wang, L.; Song, X.; Park, H.-D.; Tang, C. Y., A Critical Review on Thin-Film Nanocomposite Membranes with Interlayered Structure: Mechanisms, Recent Developments, and Environmental Applications. *Environ. Sci. Technol.* **2020,** *54*, (24), 15563–15583.

30. Lv, Y.; Du, Y.; Qiu, W. Z.; Xu, Z. K., Nanocomposite Membranes via the Codeposition of Polydopamine/Polyethylenimine with Silica Nanoparticles for Enhanced Mechanical Strength and High Water Permeability. *ACS Appl. Mater. Interfaces* **2017,** *9*, (3), 2966-2972.
31. Lv, Y.; Yang, H.-C.; Liang, H.-Q.; Wan, L.-S.; Xu, Z.-K., Nanofiltration Membranes via Co-deposition of Polydopamine/Polyethylenimine Followed by Cross-linking. *J. Membr. Sci.* **2015,** *476*, 50-58.
32. Yang, Z.; Wu, Y.; Wang, J.; Cao, B.; Tang, C. Y., In situ reduction of silver by polydopamine: A novel antimicrobial modification of a thin-film composite polyamide membrane. *Environ. Sci. Technol.* **2016,** *50*, (17), 9543-9550.
33. Guo, H.; Yao, Z.; Yang, Z.; Ma, X.; Wang, J.; Tang, C. Y., A One-Step Rapid Assembly of Thin Film Coating using Green Coordination Complexes for Enhanced Removal of Trace Organic Contaminants by Membranes. *Environ. Sci. Technol.* **2017,** *51*, (21), 12638-12643.
34. Li, W.; Shi, C.; Zhou, A.; He, X.; Sun, Y.; Zhang, J., A Positively Charged Composite Nanofiltration Membrane Modified by EDTA for $LiCl/MgCl_2$ Separation. *Sep. Purif. Technol.* **2017,** *186*, 233-242.
35. Roy, Y.; Lienhard, J. H., Factors Contributing to the Change in Permeate Quality upon Temperature Variation in Nanofiltration. *Desalination* **2019,** *455*, 58-70.
36. Roy, Y.; Warsinger, D. M.; Lienhard, J. H., Effect of Temperature on Ion Transport in Nanofiltration Membranes: Diffusion, Convection and Electromigration. *Desalination* **2017,** *420*, 241-257.
37. Labban, O.; Liu, C.; Chong, T. H.; Lienhard, J. H., Relating Transport Modeling to Nanofiltration Membrane Fabrication: Navigating the Permeability-Selectivity Trade-Off in Desalination Pretreatment. *J. Membr. Sci.* **2018,** *554*, 26-38.
38. Roy, Y.; Sharqawy, M. H.; Lienhard, J. H., Modeling of Flat-Sheet and Spiral-Wound Nanofiltration Configurations and its Application in Seawater Nanofiltration. *J. Membr. Sci.* **2015,** *493*, 360-372.
39. Labban, O.; Liu, C.; Chong, T. H.; Lienhard, J. H., Fundamentals of Low-Pressure Nanofiltration: Membrane Characterization, Modeling, and Understanding the Multi-Ionic Interactions in Water Softening. *J. Membr. Sci.* **2017,** *521*, 18-32.
40. Ahmad, A.; Ooi, B.; Mohammad, A. W.; Choudhury, J., Composite Nanofiltration Polyamide Membrane: A Study on the Diamine Ratio and Its Performance Evaluation. *Ind. Eng. Chem. Res.* **2004,** *43*, (25), 8074-8082.
41. Geraldes, V.; Alves, A. M. B., Computer Program for Simulation of Mass Transport in Nanofiltration Membranes. *J. Membr. Sci.* **2008,** *321*, (2), 172-182.
42. Bowen, W. R.; Welfoot, J. S., Modelling the Performance of Membrane Nanofiltration-Critical Assessment and Model Development. *Chem. Eng. Sci.* **2002,** *57*, (7), 1121-1137.
43. Dechadilok, P.; Deen, W. M., Hindrance Factors for Diffusion and Convection in Pores. *Ind. Eng. Chem. Res.* **2006,** *45*, (21), 6953-6959.

44. Deen, W. M., Hindered Transport of Large Molecules in Liquid-Filled Pores. *AIChE J.* **1987,** *33*, (9), 1409-1425.

45. Richards, L. A.; Richards, B. S.; Corry, B.; Schäfer, A. I., Experimental Energy Barriers to Anions Transporting through Nanofiltration Membranes. *Environ. Sci. Technol.* **2013,** *47*, (4), 1968-1976.

46. Sigurdardottir, S. B.; DuChanois, R. M.; Epsztein, R.; Pinelo, M.; Elimelech, M., Energy Barriers to Anion Transport in Nanofiltration Membranes: Role of Intra-Pore Diffusion. *J. Membr. Sci.* **2020,** *603*, 117921.

47. Tunuguntla, R. H.; Henley, R. Y.; Yao, Y.-C.; Pham, T. A.; Wanunu, M.; Noy, A., Enhanced Water Permeability and Tunable Ion Selectivity in Subnanometer Carbon Nanotube Porins. *Science* **2017,** *357*, (6353), 792-796.

48. Zhou, X.; Wang, Z.; Epsztein, R.; Zhan, C.; Li, W.; Fortner, J. D.; Pham, T. A.; Kim, J.-H.; Elimelech, M., Intrapore Energy Barriers Govern Ion Transport and Selectivity of Desalination Membranes. *Sci. Adv.* **2020,** *6*, (48), eabd9045.

49. Sun, P.-F.; Kim, T.-S.; Kim, H.-S.; Ham, S.-Y.; Jang, Y.; Park, Y.-G.; Tang, C. Y.; Park, H.-D., Improved Anti-biofouling Performance of Pressure Retarded Osmosis (PRO) by Dosing with Chlorhexidine Gluconate. *Desalination* **2020,** *481*, 114376.

50. Ham, S.-Y.; Kim, H.-S.; Jang, Y.; Sun, P.-F.; Park, J.-H.; Lee, J. S.; Byun, Y.; Park, H.-D., Control of Membrane Biofouling by 6-Gingerol Analogs: Quorum Sensing Inhibition. *Fuel* **2019,** *250*, 79-87.

51. Kim, H.-S.; Ham, S.-Y.; Jang, Y.; Sun, P.-F.; Park, J.-H.; Hoon Lee, J.; Park, H.-D., Linoleic acid, a plant fatty acid, controls membrane biofouling via inhibition of biofilm formation. *Fuel* **2019,** *253*, 754-761.

52. Zhang, L.; Wang, H.; Yu, W.; Su, Z.; Chai, L.; Li, J.; Shi, Y., Facile and Large-Scale Synthesis of Functional Poly(m-Phenylenediamine) Nanoparticles by Cu^{2+}-assisted Method with Superior Ability for Dye Adsorption. *J. Mater. Chem.* **2012,** *22*, (35), 18244.

53. Chai, L.; Wang, T.; Zhang, L.; Wang, H.; Yang, W.; Dai, S.; Meng, Y.; Li, X., A Cu–m-Phenylenediamine Complex Induced Route to Fabricate Poly(m-Phenylenediamine)/Reduced Graphene Oxide Hydrogel and Its Adsorption Application. *Carbon* **2015,** *81*, 748-757.

54. Wang, L.; Song, X.; Wang, T.; Wang, S.; Wang, Z.; Gao, C., Fabrication and Characterization of Polyethersulfone/Carbon Nanotubes (PES/CNTs) Based Mixed Matrix Membranes (MMMs) for Nanofiltration Application. *Appl. Surf. Sci.* **2015,** *330*, 118-125.

55. Yu, W.; Zhang, L.; Meng, Y.; Dai, S.; Su, Z.; Chai, L.; Wang, H., High Conversion Synthesis of Functional Poly(m-Phenylenediamine) Nanoparticles by Cu-OH-assisted Method and Its Superior Ability toward Ag^{+} Adsorption. *Synth. Met.* **2013,** *176*, 78-85.

56. Ma, L.; Qin, H.; Cheng, C.; Xia, Y.; He, C.; Nie, C.; Wang, L.; Zhao, C., Mussel-inspired Self-coating at Macro-interface with Improved Biocompatibility and Bioactivity via Dopamine Grafted Heparin-like Polymers and Heparin. *J. Mater.*

Chem. B **2014,** *2*, (4), 363-375.

57. Zhang, X.; Jia, C.; Xue, Y.; Yang, P., Fabrication of RGO/g-C_3N_4 Composites via Electrostatic Assembly towards Charge Separation Control. *RSC Adv.* **2017,** *7*, (69), 43888-43893.

58. Bowen, W. R.; Mukhtar, H., Characterisation and Prediction of Separation Performance of Nanofiltration Membranes. *J. Membr. Sci.* **1996,** *112*, (2), 263-274.

59. Košutić, K.; Dolar, D.; Kunst, B., On Experimental Parameters Characterizing the Reverse Osmosis and Nanofiltration Membranes' Active Layer. *J. Membr. Sci.* **2006,** *282*, (1-2), 109-114.

60. Wadekar, S. S.; Vidic, R. D., Influence of Active Layer on Separation Potentials of Nanofiltration Membranes for Inorganic Ions. *Environ. Sci. Technol.* **2017,** *51*, (10), 5658-5665.

61. Liang, Y.; Zhu, Y.; Liu, C.; Lee, K.-R.; Hung, W.-S.; Wang, Z.; Li, Y.; Elimelech, M.; Jin, J.; Lin, S., Polyamide Nanofiltration Membrane with Highly Uniform Sub-Nanometre Pores for Sub-1 Å Precision Separation. *Nat. Commun.* **2020,** *11*, (1), 1-9.

62. Van der Bruggen, B.; Vandecasteele, C., Modelling of the Retention of Uncharged Molecules with Nanofiltration. *Water Res.* **2002,** *36*, (5), 1360-1368.

63. Yang, G.; Shi, H.; Liu, W. Q.; Xing, W. H.; Xu, N. P., Investigation of Mg^{2+}/Li^{+} Separation by Nanofiltration. *Chinese J Chem Eng* **2011,** *19*, (4), 586-591.

64. Ben-Sasson, M.; Zodrow, K. R.; Genggeng, Q.; Kang, Y.; Giannelis, E. P.; Elimelech, M., Surface Functionalization of Thin-Film Composite Membranes with Copper Nanoparticles for Antimicrobial Surface Properties. *Environ. Sci. Technol.* **2014,** *48*, (1), 384-393.

65. Kochkodan, V.; Hilal, N., A Comprehensive Review on Surface Modified Polymer Membranes for Biofouling Mitigation. *Desalination* **2015,** *356*, 187-207.

TOC

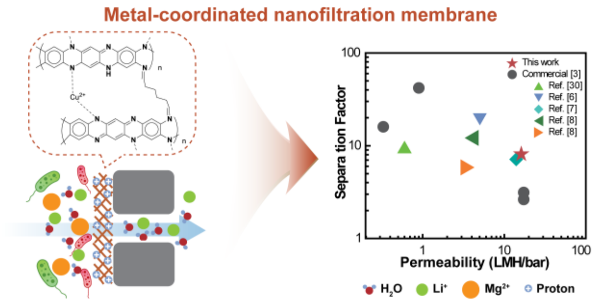

Metal-coordinated nanofiltration membrane
This work
Commercial [3]
Ref. [30]
Ref. [6]
Ref. [7]
Ref. [8]
Ref. [8]
Separa tion Factor
Permeability (LMH/bar)
100
10
1
1
10
100
H2O
Li+
Mg2+
Proton